10

Development and Application of Low-Modulus Biomedical Titanium Alloy Ti2448

Rui Yang, Yulin Hao and Shujun Li
Shenyang National Laboratory for Materials Science,
Institute of Metal Research, Chinese Academy of Sciences
P. R. China

1. Introduction

Economic development leads to improved living standard, but is also attended by the following consequences: increased number of senile people who, due to degenerative diseases such as arthritis, may need medical assistance in maintaining their convenience of mobility, increased volume of transportation in terms of the number of cars and associated traffic accidents, and increased amount of leisure time channeled to sports that have a higher than average risk of injuries. All these require orthopaedic surgeries and cause increased consumption of biomedical materials.

Load bearing orthopedic implants must satisfy the following requirements (Wang, 1996; Long & Rack, 1999): First of all they are ideally without cytotoxicity, and this places stringent restriction to the choice of alloying elements. Secondly, their long service life coupled with the variety of human activity demands excellence in mechanical properties, primarily high strength and high fatigue resistance, but low elastic modulus. This is a big challenge because for crystalline materials their strength and elastic modulus tend to increase or decrease simultaneously. Thirdly, wear resistance is important because wear causes not only implant loosening but also harmful reactions if the wear debris is deposited in the tissue. Finally, biochemical compatibility requires the implanted materials to possess superior corrosion resistance in body environment and be bioactive. The first two aspects clearly fall into the domain of alloy design; the last two, though closely related to alloy type and composition, are normally the subjects of surface modification.

Judging from the above requirements titanium alloys stand out as the best class of implant materials due to a combination of acceptable biocompatibility and good properties such as high strength, low density, relatively low elastic modulus and excellent corrosion resistance. While Ti–6Al–4V is used earliest in biomedical engineering and is still a benchmark among biomedical alloys (Froimson et al., 2007), it was not purpose-designed. In terms of cytotoxicity, vanadium is toxic both in the elemental state and in the form of oxide (Wapner, 1991; Eisenbarth et al., 2004), and there exits some correlation between V and Al ions released from the alloy and long-term health problems such as Alzheimer disease, neuropathy and ostemomalacia (Nag et al., 2005). These facts highlight the importance of careful choice of alloying additions when designing new alloys specifically for biomedical use.

The main mechanical effect of an implant on the bone relates to stress shielding, i.e., reduction in bone stress *in vivo* following the introduction of the implant. The stress needed by cells around the implant is thus shielded and the cells do not survive. The change in stress

Factor	P-value
Bending stiffness ratio	0.0002
Torsional stiffness ratio	0.0001
Stem bending stiffness	0.0150
Stem tortional stiffness	0.0140
Stem design type	0.2100
Age	0.8500
Sex	0.4700

Table 1. Statistical significance of correlation between severe stress shielding and various influencing factors (Wan et al., 1999).

distribution in the affected bone causes bone loss and originates from the mismatch of stiffness. There is a clinical study (Wan et al., 1999) showing statistical correlation between stress shielding related bone loss in hip arthroplasty and stem to bone stiffness ratio (Table 1). While stiffness of the implant can be adjusted by different design, its shape and function are normally predetermined and do not allow much variation. The main route to improve the match of stiffness between the implant and the bone then is to reduce the elastic modulus of the implant material which is normally 3 or 4 times that of the bone ($4 \sim 30$ GPa (Black & Hastings, 1998))). Recent efforts have brought the Young's modulus down to 55 GPa in the alloy Ti–29Nb–13Ta–7.1Zr but this is still almost twice that of bone (Table 2).

The titanium alloy we developed over the past few years, Ti–24Nb–4Zr–8Sn, code named Ti2448, has a record low incipient Young's modulus of 42 GPa, while maintaining a high strength of over 850 MPa (Hao et al., 2005)). The alloy has undergone a full cycle of development, biosafety examination, implant part design and manufacturing, *in vivo* tests and clinical trials. In the following, we first outline key design considerations of this low-modulus, high-strength biomedical alloy, followed by some details of alloy development and optimization. Biomechanical properties of Ti2448 will then be described, with particular attention paid to the peculiar mechanisms of elasticity. A number of surface modification strategies have been tried on this new alloy and the outcome will be briefly reviewed. We conclude this chapter after a mention of the *in vivo* and clinical test results.

Alloy	E (GPa)	Alloy	E (GPa)
CoCr (Cast)	240	Ti–13Nb–13Zr	77
AISI 316L	210	Ti–29Nb–13Ta–4Mo	74
Commercial Pure Ta	200	Ti–29Nb–13Ta–6Sn	74
Ti–6Al–4V	112	Ti–29Nb–13Ta–4.6Sn	66
Ti–6Al–7Nb	110	Ti–29Nb–13Ta–4.5Zr	65
Ti–5Al–1.5B	110	Ti–29Nb–13Ta–2Sn	62
Commercial Pure Ti	100	Ti–29Nb–13Ta–7.1Zr	55
Ti–16Nb–13Ta–4Mo	91	NiTi	48
Ti–12Mo–6Zr–2Fe	85		
Ti–15Mo–5Zr–3Al (ST) aged	80	Ti2448 (Ti–24Nb–4Zr–8Sn)	42
Ti–29Nb–13Ta–4.6Zr (aged)	80	Bone	30

Table 2. Young's modulus E of biomedical alloys compiled in a recent review (Geetha et al., 2009), in comparison with that of Ti2448 and of bone.

2. Primary design considerations

For most binary titanium alloys formed with transition metal (TM) elements the variations of their Young's moduli with solute concentration are as shown in Fig. 1. Ti–Fe is typical of the so-called β-eutectoid alloys formed with elements such as Cr, Mn, Fe, Co and Ni, while Ti–Mo is representative of the β-isomorphous alloys such as Ti–V, Ti–Mo and Ti–Nb. Roughly, the distinction between these two families of alloys is that right of the peak on the modulus curve, with increasing solute concentration, E continues to decrease (before final increase) for Ti–Fe, but increases right away for Ti–Mo. On the schematic drawing of Fig. 1c, at low e/a with decreasing solute concentration the β phase becomes less stable and the formation of the α phase or α' martensite causes the Young's modulus to increase. At high e/a the β phase is stabilized and the Young's modulus increases with solute content. The peak in the middle is essentially caused by the formation of metastable ω phase which has a higher modulus than the β. The effect of the α'' martensite is superimposed on the curve and its formation helps to shape the valley left of the peak.

In designing a new generation of biomedical titanium alloys the first principle is to exclude elements that are toxic or are allergic in human body. We use the following alloying strategy to reduce the elastic modulus: First, the alloying additions must remove the ω phase as it is not only responsible for the peak in elastic modulus but also regarded as highly undesirable due to its embrittling effects. Secondly, the alloying should ideally depress the martensite start point to below ambient temperature so that the transformation can be stress induced. This transformation can then be employed to improve superelasticity, a characteristic useful in many biomedical applications. Thirdly, it can be seen from Fig. 1 that even after the peak is removed the elastic modulus represented by the minimum on the dotted curve is still far higher than that of bone. So the alloying scheme must be able to further reduce the intrinsic elastic modulus of the β phase. Finally, of course, strength should not be compromised as a result of alloying.

A first principles method to estimate the bulk moduli of body-centred cubic metals was proposed by computing the binding energy per atom of an atomic cluster and then taking the second order derivative of the binding energy vs. unit cell volume plots at the equilibrium point (Song, Yang, Li, Wu & Guo, 1999). By constructing a cluster containing a solute the bulk modulus of β-type titanium alloys can be estimated and the results for a series of Ti–TM

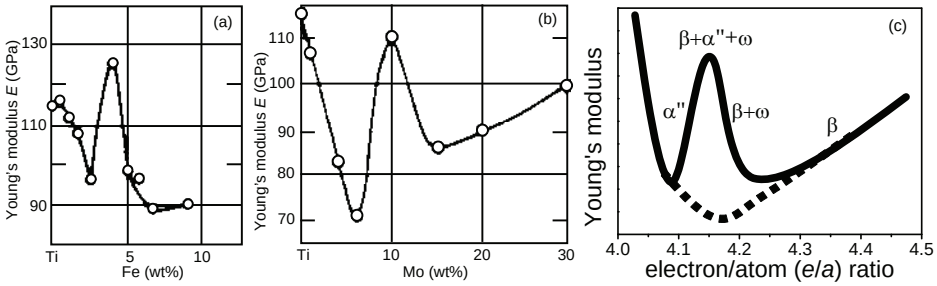

Fig. 1. Young's moduli, E, of Ti-Fe (a) and Ti-Mo (b) alloys as functions of composition (Fedotov, 1973). A schematic of the E vs. e/a plot for Ti-TM alloys is shown in (c) with the dotted curve indicating the intrinsic minimum in E of the β phase (Hao, Li, Sun, Zheng & Yang, 2007).

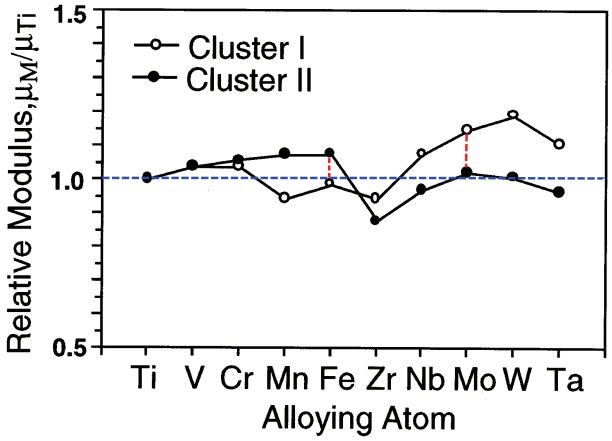

Fig. 2. Relative modulus of Ti–TM alloys to the β-Ti control. The open and solid symbols are estimates from clusters containing 15 and 27 atoms, respectively (Song, Xu, Yang, Li, Wu & Guo, 1999). Dotted lines are for guiding the eye.

alloys were reported (Song, Xu, Yang, Li, Wu & Guo, 1999). Figure 2 shows plots of the relative modulus (compared to pure β-Ti) of both β-eutectoid and β-isomorphous type alloys. Because calculations with a larger cluster take into account more atomic interactions the results are considered more reliable. It can be seen from the plot for Cluster II that Zr, followed by Nb and Ta, reduces the intrinsic modulus of β-Ti.

The change of the relative modulus for a given alloying addition for the two atomic clusters in Fig. 2 is worth noting. Because a solute atom in a smaller β-Ti cluster qualitatively corresponds to a higher solute concentration than that in a larger cluster, the computed results appear to agree with the two types of modulus curve represented by Fig. 1a and b. In Fig. 2, for the β-eutectoid alloys (e.g., Fe addition) the modulus for cluster I is smaller than for cluster II, while for the β-isomorphous alloys (e.g., Mo addition) the reverse is true (although for V, modulus values for the two clusters are similar, suggesting a slow increase in elastic modulus with increasing V addition).

In deciding the primary binary alloy system as a basis for further alloy development, we consider Ti–Zr not suitable because Zr is in the same group as Ti on the periodic table. To modify the properties that are sensitive to the c/a, such as the β phase stability, alloying with Zr is inefficient. A recent, more sophisticated first principles calculation (Hu et al., 2008) confirmed the above empirical rule. The theoretical results also show that although Zr stabilizes the β phase energetically (thermodynamically) this phase remains elastically (mechanically) unstable. Ta on the other hand is heavy and has a high melting point. As a result alloys containing Ta are prone to segregation and are more difficult and costly to melt. The high cost of elemental Ta and its high density compared to other TM metals certainly do not favour its use in biomedical alloys. The above considerations left Ti–Nb as our choice of the primary alloy system for further property improvement and composition optimization.

3. Development and optimization

Zr and Sn are very effective in suppressing the α'' martensitic transformation of alloys based on Ti–Nb, and the addition of 1 wt% of Zr and Sn reduces the martensitic start temperature

by 41.2 K and 40.9 K, respectively, as compared to 17.6 K by 1 wt% of Nb (Hao et al., 2006). First principles computations (Hu et al., 2008) suggest that the addition of Nb to Ti increases both the elastic and phase stability of the β. Our theoretical Nb concentration above which the β phase is stable is about 24 at.%, in perfect agreement with experimental values of 21 – 23 at.% (Collings, 1984; Dobromyslov & Elkin, 2001). However, a stable β phase of binary Ti–Nb (with at least 24 at.% Nb) possesses undesirbable high elastic moduli. Replacing some of the Nb with Zr suppresses the elastic moduli to a relatively low level, but Zr does not effectively improve the stability of the β phase. Adding Sn improves efficiently the phase stablity of the β while avoiding to harden most of the elastic moduli. Excessive amount of Sn, however, has the undesirable consequence of increasing $E_{\langle 111\rangle}$ and $G_{\{001\}\langle 010\rangle}$. Systematic composition optimization has to be carried out to achieve the best biomechanical properties.

Atomic interactions become more complex in multicomponent alloys and two results of the first principles computation (Hu et al., 2008) are particularly worth noting. The first is that the stabilizing effects of Sn and Zr on the β phase become weaker in the ternary alloys (containing 15 at.% Nb) than in the binary alloys. Thus the alloying effects on the phase stability of β-type titanium alloys cannot be simply superimposed. The second is the stronger β-stabilizing effect of Sn than Nb which is unexpected because Sn is commonly believed to be a weak α stabilizer while Nb certainly is a β stabilizer in most $\alpha + \beta$ two-phase alloys. This effect of Sn must be due to the new patterns of constituent phases of the β-type alloys, where the α phase has been suppressed and the rivals become metastable phases such as the ω and the α''.

Table 3 presents the constituent phases of Ti–Nb–Zr–Sn alloys with compositions in the interested range, as identified by x-ray diffraction analysis. It can be seen that for most compositions a metastable phase, either the ω or the α'', accompanies the β, but there does exist a composition range in which the β phase is sufficiently stabilized to be alone. This composition range corresponds to the dotted curve of Fig. 1c, i.e., the peak of the Young's modulus has been successfully removed. Because Ti–Nb is a β-isomorphous system we need to keep Nb content to a minimum in order to minimize the elastic modulus. Thus alloys around the composition of Ti–24Nb–4Zr–7.5Sn are of interest and potentially possess the lowest Young's modulus.

The cyclic tensile stress-strain curves of the $\beta + \omega$ and β type microstructures are compared in Fig. 3. In the former the tensile curves are normal and the alloy exhibits linear elastic deformation before plastic yield at about 1% strain. The β type microstructure, however, shows stress-strain behaviour that sharply contrasts the two-phase microstructure. The "double yield" feature characteristic of stress induced martensitic transformation is quite evident, and the shoulder on the curve corresponds to the formation of the α'' martensite during tensile straining. Recoverable strain increases to about 2% enclosing a fairly significant hysterisis loop.

	20Nb	22Nb	24Nb	26Nb
2Zr–7.5Sn			$\beta + \alpha''$	
4Zr–7.5Sn	$\beta + \alpha''$	$\beta + \alpha''$	β	β
8Zr–7.5Sn			$\beta + \omega$	
4Zr–3.5Sn	$\alpha'' + \omega$	$\alpha'' + \omega$	$\beta + \alpha''$	$\beta + \alpha''$
4Zr–11.5Sn	$\beta + \omega$		$\beta + \omega$	$\beta + \omega$

Table 3. Nominal chemical composition (wt%) and corresponding phase constitution of as-quenched Ti–Nb–Zr–Sn alloys determined by x-ray diffraction analysis (Hao et al., 2006).

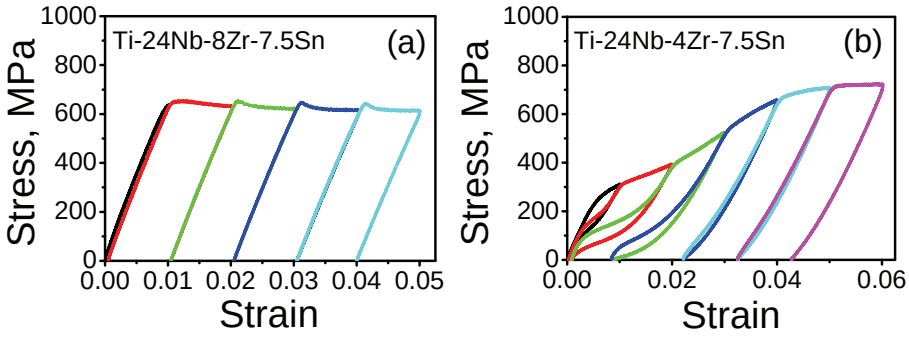

Fig. 3. Stress-strain curves at 294 K of water quenched Ti–24Nb–8Zr–7.5Sn with $\beta + \omega$ (a), and Ti–24Nb–4Zr–7.5Sn with β (b) starting microstructure.

Detailed experimental studies show that the recoverable strain and the shape of the cyclic stress-strain curve are sensitive to oxygen and Sn content. The double yield feature is most pronounced in the lower-solute alloys. At intermediate solute content of Ti–24Nb–4Zr–7.9Sn–(0.11∼0.12)O (Hao et al., 2005; Hao, Li, Sun, Sui & Yang, 2007), total recoverable strain is large and strongly nonlinear, but the characteristic form of a superelastic flow curve is smoothed such as to obscure any signs of a plateau characteristic of double yield phenomena. These alloys represent the optimized compositions and we code name them Ti2448 to reflect the nominal composition of Ti–24Nb–4Zr–8Sn.

It is worth noting that Zr is a very potent strengthener in Ti2448 whose tensile strength after hot work ranges between 690–920 MPa depending on interstitial content. This compares to a mere 460 MPa of Ti–24.3Nb–8.3Sn (Nitta et al., 2004), nearly equal to the Ti2448 composition less Zr. Removal of the stress plateau on the stress-strain curve of Ti2448 makes it particularly suitable for biomedical applications which require high strength and high fatigue endurance.

4. Biomechanical properties

As mentioned in the previous sections, key to implant applications are low elastic modulus and preferably good elasticity, as well as high strength and fatigue resistance. These biomechanical properties with reference to Ti2448 will be reviewed in this section.

First of all the definition of Young's modulus should be noted. For linear elastic behaviour the tensile Young's modulus is defined as the slope of the linear elastic range before the onset of plastic deformation. For materials exhibiting nonlinear elastic behaviour, such as β-type titanium alloys, however, linearity does not extend to the whole elastic range, and Young's modulus becomes a function of elastic strain. In such cases, *incipient* Young's modulus, which refers to the slope of tangent at zero strain on the stress-strain curve, should be differentiated from *average* Young's modulus which is defined as that of an intersection line from zero to the upper limit of fully recovered strain during unloading. Figure 4 illustrates the point with hot-rolled Ti2448 tensile strained to slightly above the fully recovered strain. Since the initial 0.5% tensile strain of Ti2448 is almost linear, incipient Young's modulus is conveniently defined as the slope of the linear elastic range up to 0.5%. This method gives better accuracy than employing the tangent at the zero strain point of the stress-strain curve. The average Young's modulus is a good measure of stiffness at large strains and is in general smaller than the incipient Young's modulus. The implant for hard tissue replacement however is not

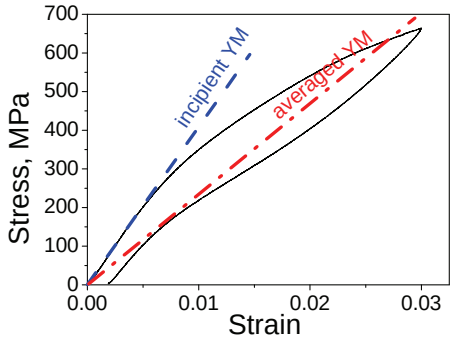

Fig. 4. Stress-strain curves of loading-unloading deformation of as hot-rolled Ti2448, illustrating definition of the Young's modulus (YM)(Hao, Li, Sun, Zheng & Yang, 2007).

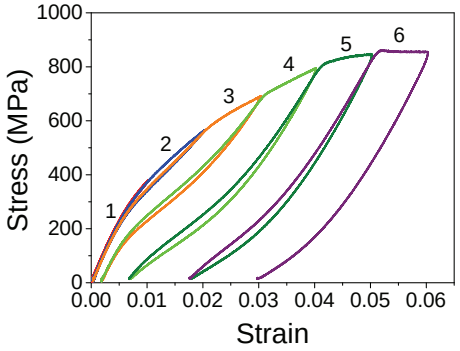

Fig. 5. Cyclic loading-unloading stress-strain curves of hot-rolled Ti2448 to a total strain of 0.06 at a strain step of 0.01 (Hao et al., 2005).

expected to undergo large deformation and the incipient Young's modulus is a more suitable quantity to describe the elastic compatibility with human bone. In this chapter, all Young's modulus, except otherwise stated, refers to the incipient Young's modulus.

The typical cyclic loading stress-strain curves of Ti2448 is shown in Fig. 5. As mentioned in the previous section, the plateau on the loci of stress-strain curves typical of double yield has completely disappeared, making it difficult to judge if stress induced martensitic transformation took place during loading. Compared to the two kinds of shapes of stress-strain curves in Fig. 3, Fig. 5 represents a new kind. Apparent from the stress-strain curves, Ti2448 does not exhibit work hardening, and the ultimate tensile strength of this particular sample (influenced by oxygen content) is 850 MPa. The cyclic straining experiment allows us to gain the following information: The recoverable strain, at about 2.8% for the virgin sample, slightly increases with prestrain to a maximum of about 3.3% in the fourth cycle. The incipient Young's modulus measured from the stress-strain curve for the first loading cycle is 42 GPa, and maintains approximately this value for the second and third cycle. For subsequent cycles with unrecoverable strains, however, the incipient Young's modulus progressively decreases, to a value of 18 GPa in the sixth loading cycle. We term this uncommon behaviour elastic softening due to prestrain.

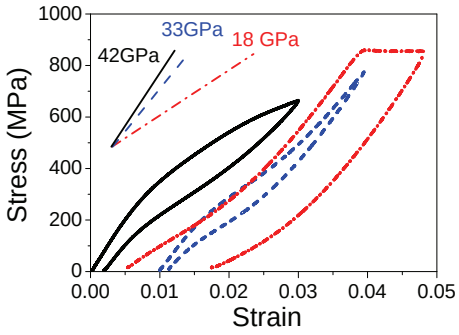

Fig. 6. Elastic softening during prestrain and recovery durign ambient temperature ageing of the as hot-rolled Ti2448. Solid, dash-dot, and dash curves are respectively single step loading-unloading (Fig. 4), the sixth cycle stress-strain curve in Fig. 5, and stress-strain curve of the same tensile sample tested 6 days after the cyclic deformation experiment, demonstrating partial recovery of incipient Young's modulus (Hao, Li, Sun, Zheng & Yang, 2007).

Even more striking is the recovery of the softened elastic modulus during ageing at room temperature, which is unusual for titanium alloys (Fig. 6). The cyclic tensile tested sample was subjected to straining experiment again after 6 days (to a strain of 0.03, see Fig. 6)) and it was observed that the incipient Young's modulus increased from 18 GPa to 33 GPa. The same experiment after 6 month on the same sample showed that the incipient Young's modulus is stabilized at about 33 GPa and does not recover in a significant way any further.

The above elastic softening due to prestrain and recovery behaviour appear to mimic the biological characteristics of human bone. With sport or movement induced strain, the incipient Young's modulus of the implant would progressively decrease to fall to the modulus range of human bone to allow complete elastic matching. During rest the implant would gradually recover its modulus to a value slightly above that of human hard tissue. Understanding of the elastic softening and recovery of Ti2448 is incomplete, but some clues to this extraordinary behaviour will be discussed in the next section.

The effects of different heat treatment on the mechanical properties of Ti2448 have been systematically investigated (Hao, Li, Sun, Zheng & Yang, 2007). Solution treatment at high temperature has weak effect on superelasticity but causes the decrease of strength and slight increase of the incipient Young's modulus (by about 8 GPa). Slower cooling (such as air cooling) causes a slight increase of tensile strength and incipient Young's modulus (3–5 GPa) and reduces the recoverable strain compared to water quenching after solution treatment. This is interpreted as a consequence of the precipitation of the α phase during slow cool. The β stabilizers such as Nb are enriched in the β phase as a result of the precipitation to make the β phase more resistant against elastic deformation and phase transformation. The formation of the α phase and increased content of Nb in the β phase both increase the elastic modulus of the alloy, as is clear from Fig. 1c. It should be noted that the ω phase that normally appears under such conditions in most β-type titanium alloys does not appear in this alloy, although it may form in alloys with different contents of alloying additions of the Ti–Nb–Zr–Sn system. For ageing treatment up to 30 min at both 723 K and 773 K, nonlinear elastic deformation is still present. Short time ageing of 10 min at both temperatures causes slight increase in both strength and incipient Young's modulus; the recoverable strain, however, seems not

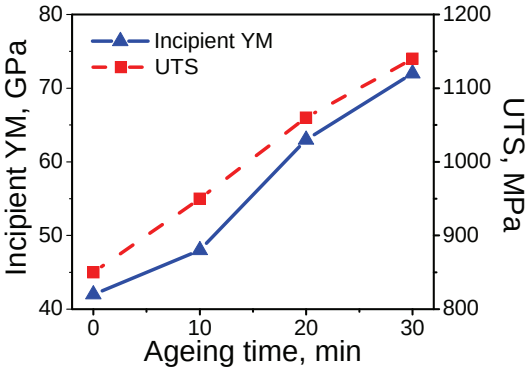

Fig. 7. Variation of the incipient Young's modulus and ultimate tensile strength with ageing time at 773 K (Hao, Li, Sun, Zheng & Yang, 2007).

affected as compared to the as hot-rolled samples. Further increase in ageing time causes the recoverable strain to decrease gradually and the elastic deformation tends to the normal linear behaviour.

Although the incipient Young's modulus increases with the increase of strength as a result of the low temperature ageing treatment, a balance of the two properties better than previously reported alloys has been achieved (Fig. 7). For the present composition, 10 min ageing at 773 K raises the incipient Young's modulus to ∼48 GPa and increases the ultimate tensile strength to 950 MPa; at a strength of ∼1150 MPa, the incipient Young's modulus is only ∼72 GPa. Under the condition of identical strength, comparison shows that Ti2448 has lower elastic modulus than previously reported β-type titanium alloys (Long & Rack, 1999; Niinomi, 2002; Matsumoto et al., 2005).

Since structural biomedical materials are used under cyclic loading conditions fatigue properties of an implant is key to its application. For materials exhibiting the double yield phenomenon during tensile testing, the first yield corresponds to the critical stress to trigger the α'' martensitic transformation from the β phase. This exceptionally low strength of the first yield raises concern over the endurance life of implants of such materials in human body. Because of the significant effect of Sn in depressing the martensitic start temperature, a reduction of Sn content over Ti2448 would produce the double yield as can be seen from Fig. 3b. Interstitial oxygen in the β is known to increase its phase stability against martensitic transformation. We have studied the fatigue properties of an alloy with the composition of Ti–24Nb–4Zr–7.6Sn–0.07O (instead of the normal ∼0.11 O) ((Li, Cui, Hao & Yang, 2008)). The obtained data should represent the lower bound of the fatigue properties of Ti2448.

The fatigue endurance limit of the hot-forged 7.6Sn alloy is comparable to that of commercial pure titanium but lower than that of Ti–6Al–4V ELI. In 0.9% NaCl the 7.6Sn alloy performs slightly better than in air in the low cycle regime. Ageing treatment at 673 K for 4 h, allowing the α phase to precipitate, increased the fatigue limit of the 7.6Sn alloy to higher than 425 MPa, which is comparable to the fatigue limit of Ti–6Al–4V ELI. This increase in fatigue strength is largely due to increased resistance to the fatigue crack initiation and to small fatigue crack propagation (Niinomi, 2003). The fatigue resistance of the cold-rolled sheets is ∼50% higher than the hot-forged bars and the data are compared to Ti–6Al–4V ELI in Fig. 8. Cold-processing techniques such as rolling and swaging are reasonable options to improve fatigue properties of this material (∼375 MPa in the case of cold rolling). Increasing

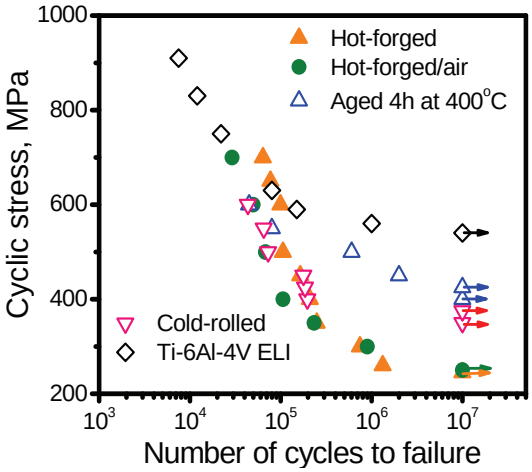

Fig. 8. *S-N* curves of Ti–24Nb–4Zr–7.6Sn tested in 0.9% NaCl except that noted in air. Data of the hot-forged Ti–6Al–4V ELI are also shown for comparison (Li, Cui, Hao & Yang, 2008).

the contents of both Sn and oxygen are effective measures to increase the fatigue strength of this class of alloys. The combination of composition optimization and heat treatment leads to a much better balance of strength, modulus and fatigue endurance in Ti2448 than Ti–6Al–4V ELI. In applications where fatigue endurance property is critical, for example, Ti2448 can be heat treated to a strength range of 1000 to 1150 MPa (with corresponding incipient Young's modulus of 60 to 72 GPa, see Fig. 7), ensuring higher high-cycle fatigue life than Ti–6Al–4V ELI while gaining the benefit of a 35% to 45% reduction in the incipient Young's modulus.

Strain-controlled low cycle fatigue properties of the hot-forged 7.6Sn alloy and Ti–6Al–4V ELI were investigated at a strain ratio 0.1 and a frequency of 0.5 Hz in air at room temperature. Figure 9 compares the maximum cyclic strains plotted against the number of cycles to failure, and it can be seen that a linear relation is obtained for both alloys. The 7.6Sn alloy shows a much higher fatigue resistance than Ti–6Al–4V ELI in the strain-controlled fatigue test. For cyclic strains between 0.25% and 2.5%, in particular, the 7.6Sn alloy reaches $\sim 4\times10^4$ cycles to failure but Ti–6Al–4V ELI withstands only $\sim 6\times10^2$ cycles.

The cyclic stress-cycle curves of the 7.6Sn alloy is compared to Ti–6Al–4V ELI in Fig. 10. For the 7.6Sn alloy, at low strains ($<\sim$3.5%), an obvious cyclic hardening after the initial cyclic softening can be observed, while the softening trend continues at high strains ($>\sim$4.0%). Ti–6Al–4V ELI, on the other hand, exhibits no hardening for all strains in the studied range larger than $\sim$2.5% (well beyond its elastic limit of $\sim$0.6%). The cyclic hardening of the 7.6Sn alloy is not fully understood yet, and is believed to be related to the stress induced α'' martensitic transformation as well as the heterogeneous formation of a tiny amount of the ω phase at high cycles (Li, Cui, Hao & Yang, 2008).

Figure 11 compares the hysteresis loops of the 7.6Sn alloy and Ti–6Al–4V ELI with a maximum strain of $\sim$2.5%. The hysteresis loop per cycle of the 7.6Sn alloy is not symmetrical and the plastic strain per cycle is much smaller than that of Ti–6Al–4V ELI. The cycle numbers to failure (N_f) and the plastic strain per cycle ($\Delta\varepsilon_p$) of both alloys can be fitted to the Coffin-Manson equation (Puska & Golovin, 1985): $N_f^{\gamma}\Delta\varepsilon_p = C$, in which γ and C are constants related to the elongation to fracture of material in static loading. The obtained values of these

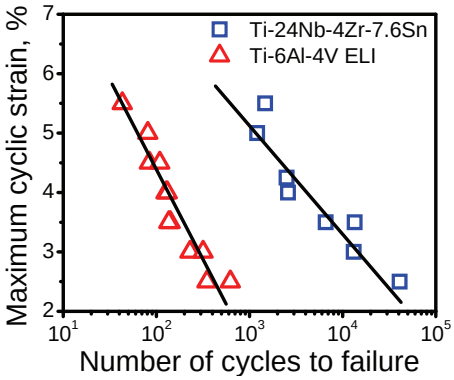

Fig. 9. Low cycle fatigue curves of as-forged Ti–24Nb–4Zr–7.6Sn and Ti–6Al–4V ELI tested in air (Li, Cui, Hao & Yang, 2008).

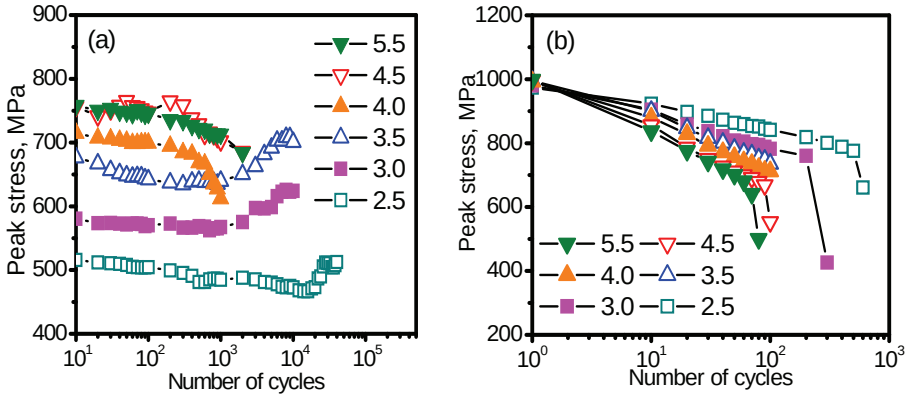

Fig. 10. Cyclic stress response curves of as-forged Ti–24Nb–4Zr–7.6Sn (a) and Ti–6Al–4V ELI (b) at different maximum strains (in percent) (Li, Cui, Hao & Yang, 2008).

two parameters for the 7.6Sn alloy are 0.46 and 0.22, respectively, both much lower than those for Ti–6Al–4V ELI (0.72 and 1.21, respectively). The low values of the $\Delta\varepsilon_p$ and γ are in accord with materials exhibiting superelastic deformation behaviour.

The beneficial effects of low incipient Young's modulus on implant robustness have been demonstrated by a study of biomechanical properties of lumbar interbody fusion cages made of the 7.6Sn alloy and Ti–6Al–4V, with incipient Young's modulus of 50 GPa and 110 GPa, respectively (Zhu et al., 2009). Both types of cages were found to be able to withstand identical compression load of ~9.8 kN (much larger than the physiological load of human body) and endure fatigue cycles beyond 5×10^6 without functional or mechanical failure under 2.0 kN axial compression. The anti-subsidence capability of both group cages was examined by axial compression of thoracic spine specimens dissected freshly from the calf with average age of 6 months. The stiffness of the vertebral bodies (K_v), which reflects resistance of the cage against subsidence, determined from this study for the 7.6Sn alloy and Ti–6Al–4V is 724 ± 8 N/mm and 527 ± 14 N/mm, respectively. These results demonstrate a clear advantage of the

low modulus alloy over conventional Ti–6Al–4V in biomechanical performance for interbody fusion cage applications.

5. Elastic and plastic deformation

The record low incipient Young's modulus of Ti2448 is a result of its peculiar elastic constants. These elastic properties also lead to new mechanisms of elastic deformation as well as unusual plastic behaviour, as will be reviewed in the following.

5.1 Elastic deformation

As mentioned in the previous sections, the widely accepted mechanism of elastic deformation in β-type titanium alloys is stress induced α'' martensitic transformation. While the double yield feature is apparent in the 7.5Sn (Fig. 3b) and 7.6Sn alloys, it is not observable for Ti2448 (Fig. 5), although after plastic deformation the α'' phase could be detected by x-ray diffraction (Hao et al., 2005). These results suggest that the stress induced phase transformation in Ti2448 possesses new characteristics compared with commonly observed α'' martensite.

It should be noted that both the β and the α can be regarded as special cases of the orthorhombic structure of the α'' phase, and can be achieved by changing the principal strains of the orthorhombic unit cell and atomic shuffle of the basal plane of $(110)_\beta \parallel (010)_{\alpha''}$ (Bendersky et al., 1994). The principal strains of the invarant plane strain transformation β-α'' can be reduced through alloying ((Hao et al., 2006)), to such a degree that the α'' phase cannot be detected by lab-scale x-ray diffraction during *in situ* straining experiment. This is true for both Ti–30Nb–10Ta–5Zr (Obbard et al. (2010)) and Ti2448 (Hao, Li, Sun, Sui & Yang (2007); Obbard (2010)). Only with synchrotron x-ray diffraction could such a stress induced transformation be detected.

Detailed analysis of synchrotron x-ray diffraction of *in situ* tensile experiment with Ti2448 sheds light on the stress induced phase transformation process. The thoroughness of shuffle of the $(110)_\beta$ atomic planes is much less in Ti2448 than in binary Ti–Nb alloys: the fraction of those achieving complete shuffle is only $0.26 \sim 0.43$ for Ti2448, but $0.60 \sim 0.83$ for binary Ti–Nb (Obbard et al. (2011)). Interstitial oxygen reduces both the degree of $(110)_\beta$ shuffle and the principal strains of the β-α'' transformation, to the effect that the critical stress for the α'' formation is increased, and stress plateau on the stress-strain curves is shortened. On the

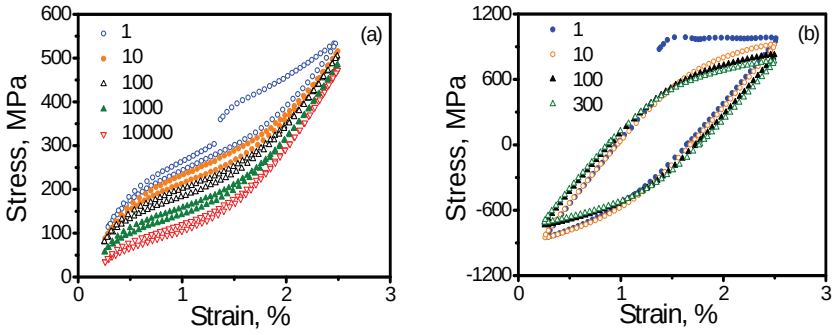

Fig. 11. Hysteresis loop of as-forged Ti–24Nb–4Zr–7.6Sn (a) and Ti–6Al–4V ELI (b) recorded at different cycles of maximum strain 2.5% during the low cycle fatigue test (Li, Cui, Hao & Yang, 2008).

other hand, the habit plane of the α'' transformation in Ti2448, $\{755\}_\beta$, is of relatively high symmetry, making the stress plateau even steeper than other alloys. These two factors lead to the disappearance of the double yield feature on the stress-strain curves of Ti2448.

Figure 12 compares the experimental stress-strain curves of both the 7.6Sn alloy and Ti2448 with theoretical ones obtained by sophisticated modelling based on synchrotron x-ray diffraction data and a model of α'' phase transformation (Obbard et al. (2011)). With increasing stress the mechanisms of recoverable strain of thermoelastic martensitic materials include martensitic shape change, detwinning of martensitic variants (Gao et al. (2000)), and martensite reorientation (Heinen et al. (2009)). The above model accounts for only the first mechanism. The detwining mechanism could reasonably be discounted here because of the small probability of twinned variants in Ti2448 due to the small transformation strains. The theoretical curves in Fig. 12 can be seen to depict the main features of the experimental curves and the agreement is better for the 7.6Sn alloy. The difference is larger for Ti2448, with the experimental strain higher than the theoretical one, and can be partly attributed to the omitting of the martensite reorientation mechanism. Other mechanisms to be discussed below also contribute to the difference. The theoretical model assumes a critical stress for the start of the transformation below which the stress-strain relation is linear. This is seen clearly from Fig. 12 to be in disaccord with experiment.

Figure 13 shows the change in peak width of $\{110\}_\beta$ and $(021)_{\alpha''}$ during 3 load cycles for both the 7.6Sn alloy and Ti2448. The difference between the two alloys is that the $(021)_{\alpha''}$ peak for the 7.6Sn alloy is sharp and its width decreases during loading; that for Ti2448 however is wide and the width tends to increase during loading below the nominal yield stress (Fig. 13d,e) while the peak width decreases during loading above the nominal yield stress (Fig. 13f). These results indicate that the α'' transformation in the 7.6Sn alloy is relatively easy to judge but it is much more difficult in the case of Ti2448. Other forms of deformation, such as precursor transformation and decomposition of the parent phase, cannot be ruled out.

The departure from linear elasticity at low applied stress before the onset of the α'' transformation may also be due to lattice distortion of the β phase. Figure 14 compares the bulk and shear moduli of Ti2448 with typical solid materials (Hao, Li, Sun, Sui & Yang (2007)). The bulk modulus of Ti2448, at 23.9 GPa, clearly reaches a record low value; and it is almost identical to the shear modulus. Low bulk modulus and Young's modulus correspond to low ideal strength and it was estimated that the β phase of Ti2448 has an ideal strength of $\sim$ 1.6 GPa. The difference between such an ideal strength and a tensile strength of 800$\sim$900 MPa is

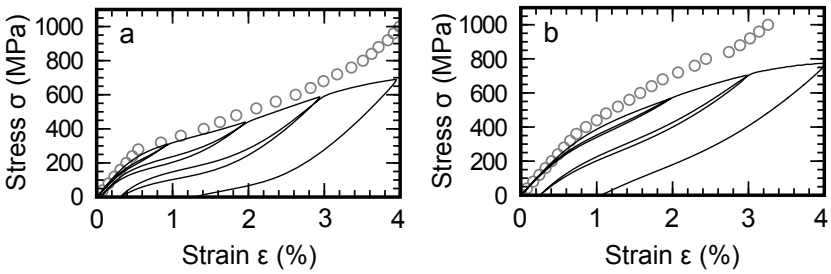

Fig. 12. Cyclic stress-strain plots (solid lines) and strain (circles) calculated using a phase transformation model applying texture and crystallography observed through synchrotron x-ray diffraction: (a) Ti–24Nb–4Zr–7.6Sn–0.08O; (b) Ti–24Nb–4Zr–8Sn–0.15O (Obbard et al., 2011).

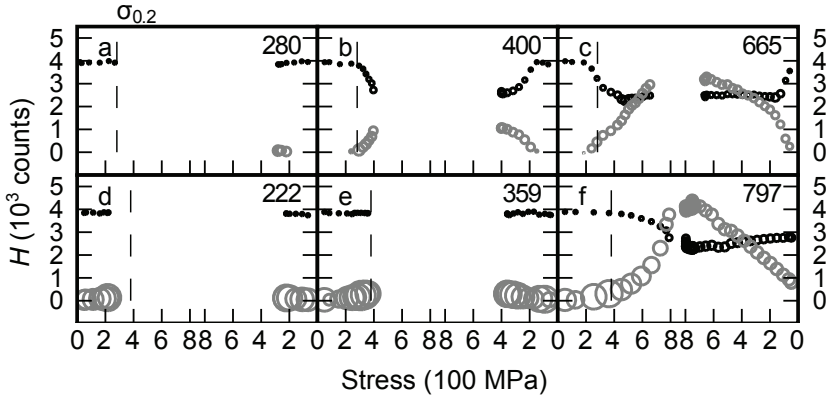

Fig. 13. Height and width of diffraction peaks over three consecutive load cycles for Ti–24Nb–4Zr–7.6Sn–0.08O (top) and Ti–24Nb–4Zr–8Sn–0.15O (bottom). Dark and light symbols show normalised H of $\{110\}_{\beta}$ and the absolute H of $(021)_{\alpha''}$. Radius of symbols is proportional to peak half-width-half-maximum; vertical lines mark nominal yield stress measured from stress-strain curves; inset stress is maximum (in MPa) for given cycle (Obbard et al., 2011).

therefore very small, leading to postulation that the β phase is approaching its limit of elastic stability in Ti2448 under applied stress. Because bulk modulus is a measure of resistance against bond length change a low value suggests more significant elastic softening under hydraulic tensile stress. Such softening would contribute to the nonlinear elastic deformation of Ti2448 below the critical stress for α'' phase transformation.

The peculiar elastic properties of Ti2448 are expected to modify its plastic deformation behaviour as will be discussed in the next subsection. A condition for dislocation based plasticity is bulk modulus being larger than shear modulus which is true for most structural metals. To investigate dislocation behaviour we choose the 7.6Sn alloy which has a higher bulk modulus (43 GPa) than Ti2448 and a shear modulus of 21 GPa. During *in situ* tensile test under high-resolution transmission electron microscopy, dislocation loops were found to nucleate homogeneously from the β phase and these loops may expand under applied

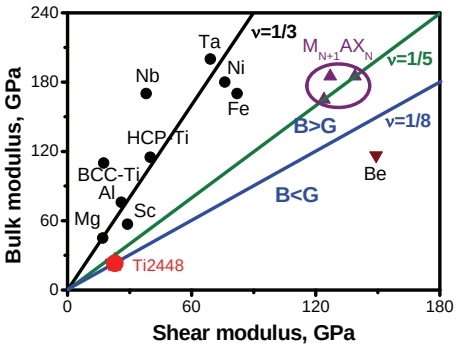

Fig. 14. A collection of shear and bulk moduli of some metals and metal-like ceramics $M_{N+1}AX_N$ in comparison with Ti2448 (Hao, Li, Sun, Sui & Yang, 2007).

stress, and shrink when the sample was held (stress relaxation) to complete disappearance (Fig. 15) (Cui et al., 2009). Dislocations normally nucleate heterogeneously at crysal defects that supply the enery needed to overcome the nucleation barrier. Homogeneous nucleation of dislocations is quite unusual and the energy needed in this case is probably supplied by the significant lattice distortion prior to the nucleation event. The reversible process of the formation and annihilation of the dislocation loops means that this plastic event has become an elastic mechanism. This novel mechanism contributes to the nonlinear elastic deformation prior to the stress induced α'' martensitic transformation.

Because the structural difference between the β and the α'' phase in Ti2448 is much reduced compared to Ti–Nb binary alloy, it is very difficult to judge experimentally when the martensitic transformation starts during loading. For the 7.6Sn alloy with slightly larger transformation strains (compared to Ti2448), differential scanning calorimetry managed to detect a peak due to the transformation. For Ti2448 which exhibits a more sluggish transformation to the α'', no peak of the new phase could be detected using this technique. It should be pointed out that the different mechanisms of elasticity may have originated from the same characteristics of the parent phase. A low energy phonon mode ($T_1\frac{1}{2}[110]$) can be noted on the phonon dispersion curves of pure titanium at 1293 K (Petry et al., 1991). This phonon mode may be softened further to a local minimum as a result of alloying and it is likely the common origin of the different modes of elastic deformation. In fact, the homogeneously nucleated dislocation loops observed in the 7.6Sn alloy are of the $k[1\bar{1}0](110)$ type, and a structure based on a stack of these loops is rather similar to the early stage of the α'' phase. These mechanisms of elasticity are therefore closely related to each other but clarifications of the specific links and delicacies require further investigation.

5.2 Plastic deformation

Plastic deformation of Ti2448 exhibits peculiar features that have not been observed in other metals. At a compression ratio of only 50% at a strain rate of $\sim 1\ s^{-1}$, highly localized plastic zones were observed in the deformed samples, leading to significant rotation of local volume and rapid grain refinement (Fig. 16). In Fig. 16a, for example, sandwiched between two nanostructure bands, local volumes rotate by almost 29 degrees (from $\sim$[111] to $\sim$[113]) in a spatial span of 1 μm. In Fig. 16b, the top and bottom regions of the view field (belonging to the same original grain) become amorphous and nanocrystalline, respectively.

The extraordinary behaviour of plastic deformation of Ti2448 has its origin in the elastic properties. Because bulk modulus and shear modulus respectively represent resistance

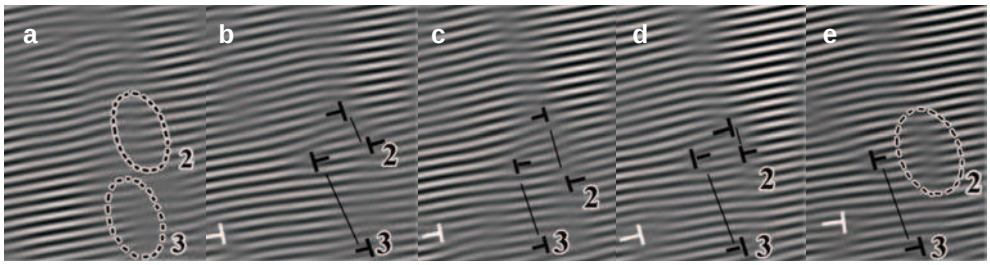

Fig. 15. Frames from a recorded digital video of a high-resolution transmission electron microscope observation of *in situ* tensile test of Ti2448, showing nucleation, expansion and shrinking of a dislocation loop (marked 2). The relative time from (a) to (e) is 0 s, 0.12 s, 0.2 s, 0.24 s, and 0.32 s (Cui et al., 2009).

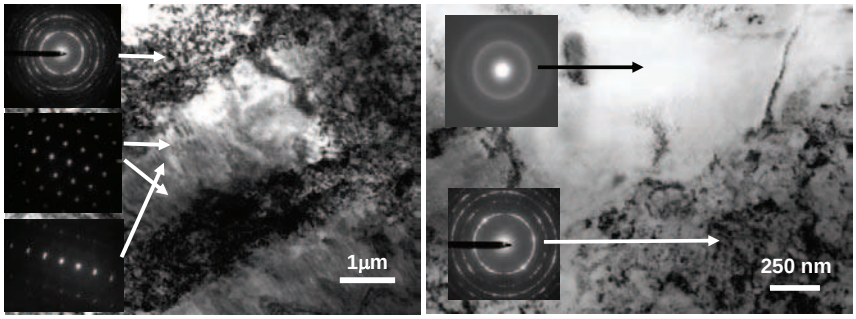

(a) (b)

Fig. 16. Bright-field transmission electron micrographs of hot-rolled Ti2448 after 50% compression. (a) Nanostructure band (indicated by diffraction pattern of top inset) and heavily rotated region (indicated by diffraction patterns of middle and bottome insets, close to zone axis [111] and [113], respectively) (Hao et al., 2005); (b) amorphous (top) and nanostructured (bottom) regions (Hao, Li, Sun, Zheng & Yang, 2007).

against changes in atomic bond length and bond angle, approximately equal values of the two elastic moduli imply that under an applied tensile stress atomic bonds in a local volume exhibit simultaneous tendencies to dilate and to rotate, rather than the domination of uniform rotation that leads to domination by shear deformation in the plastic stage in crystals whose bulk modulus is significantly greater than shear modulus (Fig. 17). In other words, atoms in a local volume undergo rather confusing and chaotic movement under an applied stress, and if the strain rate exceeds the rate for atomic relaxation, amorphous state may result, as was observed experimentally.

A mechanism of severe local lattice rotation is envisaged in Fig. 18a, with a stack of aligned dislocation loops, forming effectively a disclination type defect. At low density these loops act as a mechanism of elastic deformation as described in the previous subsection, at high density or after the loops are expanded to a sufficient size, these loops are no longer able to shrink and

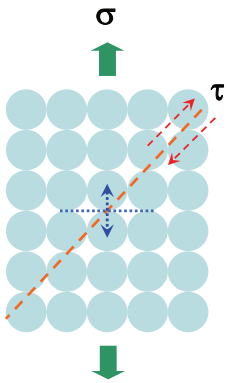

Fig. 17. Schematic illustrating atomic bond breaking across the dot line or atomic shear along the dash line, depending on the relative values of bulk modulus *B* and shear modulus *G*.

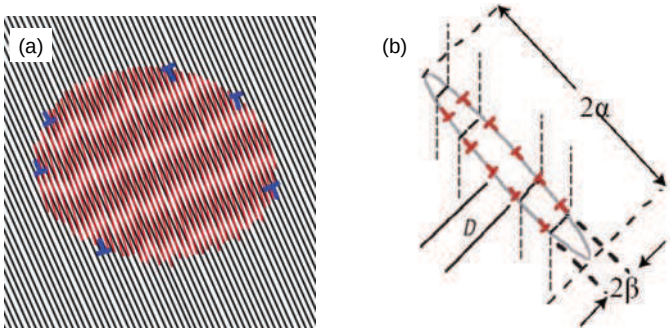

Fig. 18. (a) Schematic illustrating (a) rotation of a local volume through stacked dislocation loops (Cui et al., 2009), and (b) the incipient kink band mechanism (Barsoum et al., 2003).

they undertake plastic deformations. This mechanism can be compared to the incipient kink band that is proposed to interpret the deformation behaviour of hexagonal metals or ceramics which effectively have one easily operative slip system, loaded parallel to the basal plane. Our recent study of Ti2448 single crystals (Zhang, 2010) shows that the $C' = (C_{11} - C_{12})/2$ of the β phase is only 10.55 GPa, a record low among β-type titanium alloys. This, together with a high elastic anisotropy factor ($2C_{44}/(C_{11} - C_{12})$), makes the (110) atomic plane of the β phase the easist to shear or shuffle.

Figure 19a shows an image of nanosized grains of Ti2448 after cold rolling. Interestingly the activation energy for grain growth is different on both sides of the $\beta/(\alpha + \beta)$ transus of 923 K, being much lower on the low temperature, two-phase side (Fig. 19b). This was interpreted as a result of the nonequilibrium nature of the grain boundaries in the cold-rolled state, which is to a large extent retained during annealing in the two-phase field, but is destroyed by high temperature annealing in the β field. The very low elastic stability of the β phase in Ti2448 appears to produce a rich spectrum of metastable states. The energy barriers between these different states, either metastable phase or deformation induced defect structure, are small, making it relatively easy for transformation between these states to occur. This is the basis of the partial recovery of incipient Young's modulus at room temperature after prestrain (Fig. 6).

6. Biochemical properties and surface modification

In general surface modification methods that improve biocompatibility of titanium alloys can be used without problem on Ti2448. For example, Fig. 20 compares the cell attachment and growth behaviour of commercial pure Ti with the 7.6Sn alloy with and without hydroxyapatite coating. In this case the coating was prepared by immersion in a KOH solution followed by a heat treatment. The cell culture experiment clearly shows that the apatite layer favours adhesion and proliferation of rat osteoblast as compared to the naked samples. The uncoated 7.6Sn alloy behaves similarly to commercial pure Ti.

A two-step procedure involving thermal treatment and hydrothermal treatment for Ti2448 was also developed. Figure 21a compares the surface energy of differently treated samples. The difference in efficiency of the single-step and two-step procedure is apparent from Fig. 21c and d with the naked surface (Fig. 21b) as a reference. The surface layer resulting from the two-step procedure is both hard and bioactive.

A technique featuring the roles of the specific alloying additions of Ti2448 is micro-arc oxidation plus heat treatment. A calcium acetate electrolyte was used and the surface oxide

consists of two layers: a thin, compact and uniform inner layer and a porous outer layer. Ca ions are incorporated into the oxide layer in the form of CaO while Ti, Nb and Sn participate in the oxidation to form TiO_2, Nb_2O_5 and SnO_2, respectively. Subsequent heat treatment improves the apatite forming ability, and *in vitro* cell test on rabbit osteoblast shows that these surfaces are improved considerably in cell proliferation (Fig. 22).

A long-standing controversy concerns the relation between the grain size of metallic implant materials and biocompatibility (Hao et al., 2008). It has been speculated that refined grain size in the nanometer range improves biocompatibility but systematic investigation providing convincing proof has not been carried out, probably due to difficulty in obtaining nanostructured materials of useful dimension. Ti2448 which is easily processed into nanometer range grain size was employed to clarify this issue, and the biocompatibility of samples with 100 μm (CT) and 100 nm (NT) grain size was comparatively studied ((Zheng, 2009). Figure 23 compares the atomic force images of the two types of samples, an analysis of which yields surface roughness values of 1.45 nm and 1.94 nm for the CT and NT, respectively. Similarly, the surface energy of the CT and NT is 39 $J \cdot m^{-2}$ and 45 $J \cdot m^{-2}$, respectively (Fig. 24a), while the contents of hydroxy group on the surface of the NT sample are 69% higher

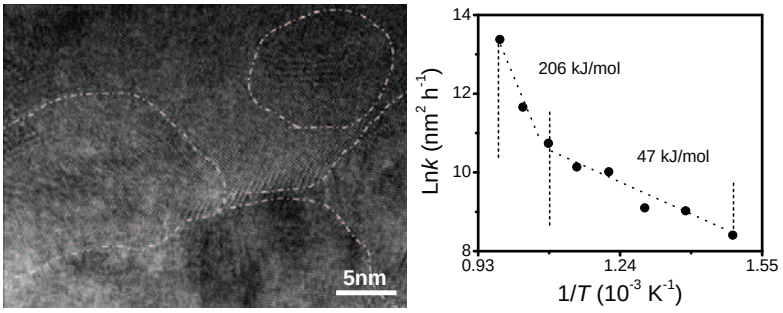

(a) (b)

Fig. 19. (a) High-resolution transmission electron micrograph showing nano-size grains of as cold-rolled Ti2448, with grain boundaries delineated by white curves; (b) Arrhenius plot of the rate constant k for grain growth against reciprocal of annealing temperature (Li, Zhang, Sun, Hao & Yang, 2008).

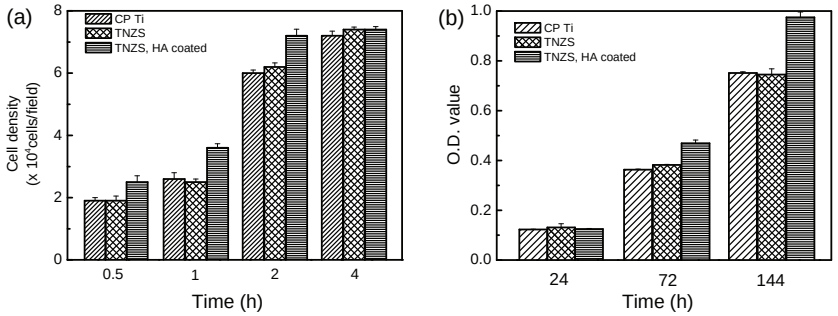

Fig. 20. Cell attachment (a) and cell growth rate (b) of Ti–24Nb–4Zr–7.6Sn (TNZS), HA-coated TNZS compared to CP Ti (Zheng et al., 2007).

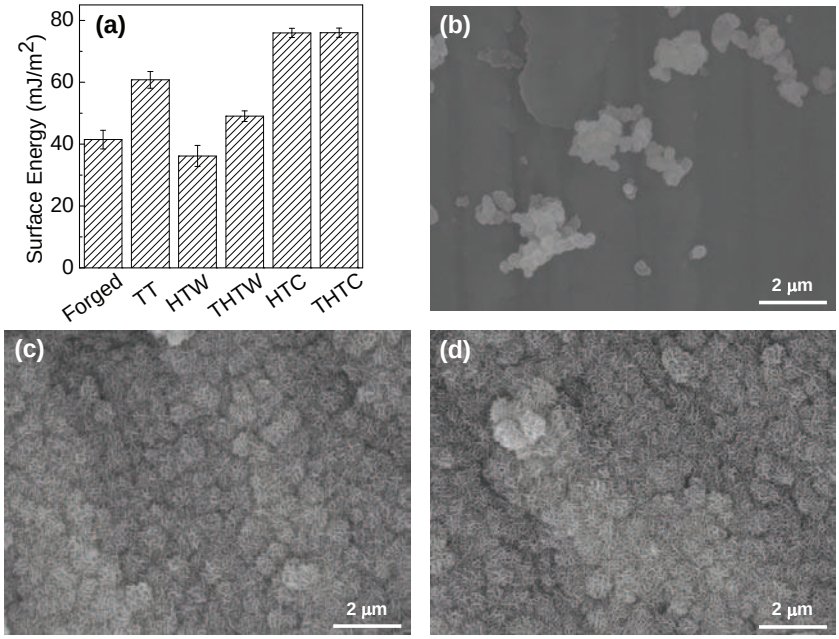

Fig. 21. (a) Surface energies of differently treated Ti2448 samples (TT: thermal treated; HT: hydrothermal treated; THT: thermal plus hydrothermal treated; W and C indicate the media of distilled water and supersaturated $Ca(OH)_2$ solution, respectively). The apatite morphologies of samples soaked in simulated body fluid are shown in the micrographs: (b) as-forged condition for 30 days; (c) HTC for 15 days; (d) THTC for 3 days (Zheng et al., 2009).

than that of the CT sample (Fig. 24b). This investigation also found that, under identical condition, the time required to form a whole layer of hydroxyapatite on the surface is 28 days for the CT sample, but only 21 days for the NT sample, and thus provided definitive evidence of the beneficial effect of surface nanostructure on the integration of titanium alloys and human tissues.

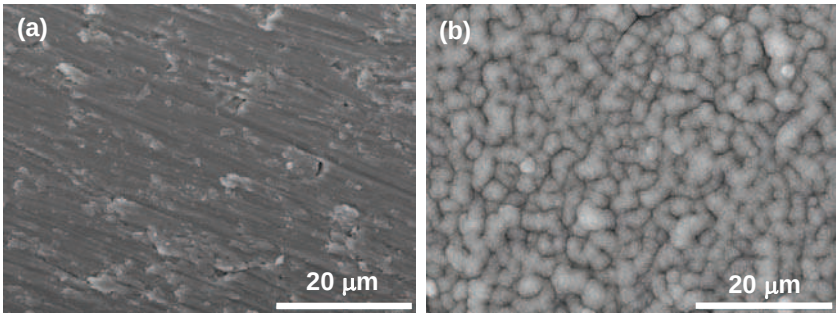

Fig. 22. Scanning electron micrographs showing apatite morphologies after soaking in simulated body fluid at 310 K for 1 week: (a) untreated surface; (b) micro-arc plus heat treated surface (Tao et al., 2009).

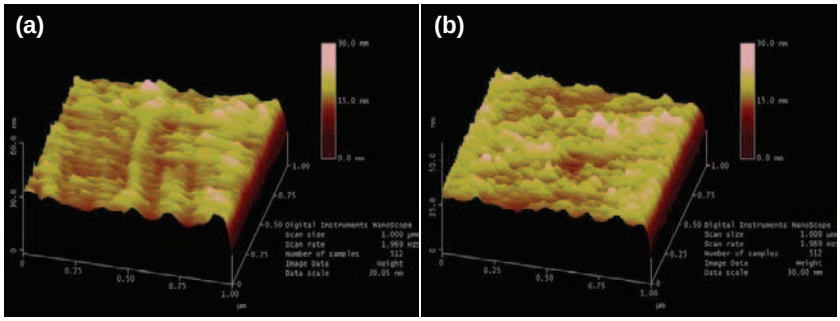

Fig. 23. Atomic force microscope images of surfaces with (a) 100 μm grain size and (b) 100 nm grain size of Ti2448 (Zheng, 2009).

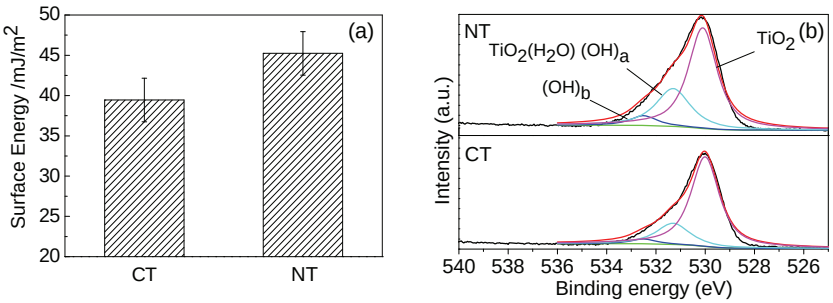

Fig. 24. (a) Comparison of surface energy of CT and NT samples; (b) x-ray photoelectronic spectrum O 1*s* peaks obtained from CT and NT samples (Zheng, 2009).

7. *In vivo* Tests and clinical trials

Extensive *in vivo* tests of Ti2448 have been conducted in the past few years in order to investigate the correlation of elastic matching between bone and implant to the healing of fractured bone. In a recent report ((Guo et al., 2009)), for example, intramedullary nails made of Ti2448 were implanted in New Zealand white rabbits in order to study the bone healing and stability of implants. It was found that the low modulus of Ti2448 leads to significant improvement in new bone formation in fractured rabbit tibiae as compared with the control group made of Ti–6Al–4V ELI (Fig. 25). These results suggest that, in the early days of fixation, nails made of low modulus Ti2448 improved new bone formation in the marrow cavity.
Clinical trials of a number of implant parts made of Ti2448, such as bone plates, nails, and spinal fixtures, have been completed. Two examples featuring repair of ankle bones and spine are shown in Figs. 26 and 27. A license application was submitted to the State Food and Drug Administration of China for large-scale production of these parts.

8. Concluding remarks

Employing a methodology that combines first principles computations of alloying effects and physical metallurgy principles, we developed a biomedical titanium alloy, Ti2448, that possesses an incipient Young's modulus of 42 GPa and a high tensile strength of over 850 MPa. The progressive softening of the incipient Young's modulus with prestrain and the ability to

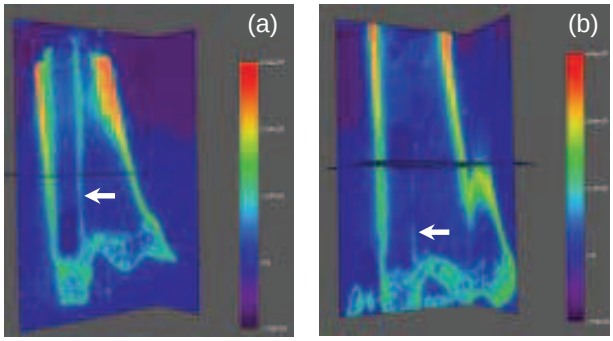

Fig. 25. Micro-CT view of (a) Ti2448 and (b) Ti–6Al–4V nails 4 weeks after implantation in rabbit tibiae. Newly formed bones are indicated by arrows (Guo et al., 2009).

recover during ambient temperature relaxation mimic the biological functions of human bone. A number of implant parts made of Ti2448 have completed clinical trials.
Ti2448 possesses superelasticity that involves new mechanisms of significant lattice distortion and homogeneous nucleation of dislocation loops in addition to stress induced martensitic

Fig. 26. Clinical application of Ti2448 bone plates and nails in repairing broken ankle bones.

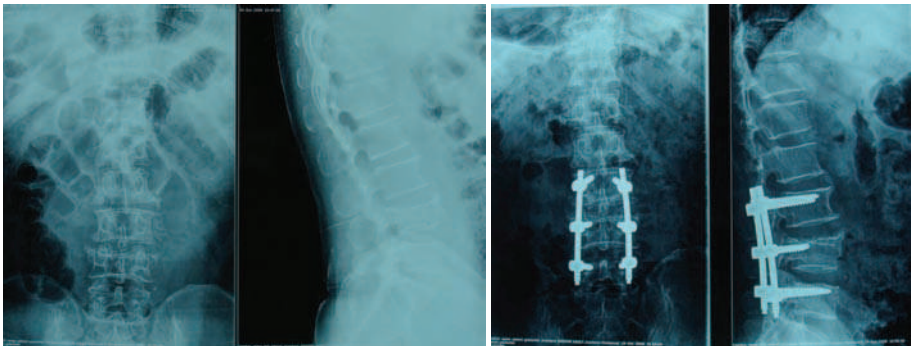

Fig. 27. Clinical application of Ti2448 implants used to repair a broken spine.

transformation. To what extent these mechanisms operate remains to be understood. We found clues to the peculiar plastic deformation that leads to rapid grain refinement of Ti2448 but the details need to be clarified. How these deformation characteristics influence biomechanical performance of implants, such as fatigue, needs systematic investigation.

9. Acknowledgement

The work was supported in part by the National Science Foundation of China grants 59925103 and 50631030, and the Ministry of Science and Technology of China grants TG2000067100 and 2006CB605104. We were drawn to the subject of titanium alloys as biomedical materials more than 10 years ago through interesting interactions with Professor Z.-X. Guo, now at University College London, and Professor Mitsuo Niinomi, now at the Institute for Materials Research, Tohoku University. We would like to thank our collaborators, Professor Zheng Guo of the Fourth Military Medical University, Professor Yue Zhu of China Medical University, and our industrial partner, Weigao Group, for their efforts in making the application of Ti2448 implants a reality. Particular thanks also go to our colleague Professor Qingmiao Hu and our former colleagues, Professors Yan Song (now at Harbin Institute of Technology at Weihai) and Manling Sui (now at Beijing University of Technology), whose valuable input has enriched our understanding of the extraordinary behaviour of β-type titanium alloys.

10. References

Barsoum, M., Zhen, T., Kalidindi, S., Radovic, M. & Murugaiah, A. (2003). Fully reversible, dislocation-based compressive deformation of Ti_3SiC_2 to 1 GPa, *Nature Mater.* 2: 107–111.

Bendersky, L., Roytburd, A. & Boettinger, W. (1994). Phase transformations in the $(Ti,Al)_3Nb$ section of the Ti–Al–Nb system — I. microstructural predictions based on a subgroup relation between phases, *Acta Metall. Mater.* 42: 2323–2335.

Black, J. & Hastings, G. (1998). *Handbook of biomaterials properties*, Chapman and Hall, London.

Collings, E. (1984). *The Physical Metallurgy of Titanium Alloy*, ASM, Metals Park, OH.

Cui, J. P., Hao, Y. L., Li, S. J., Sui, M. L., Li, D. X. & Yang, R. (2009). Reversible movement of homogenously nucleated dislocations in a β-titanium alloy, *Phys. Rev. Lett.* 102: 045503.

Dobromyslov, A. V. & Elkin, V. A. (2001). Martensitic transformation and metastable β-phase in binary titanium alloys with d-metals of 4–6 periods, *Scripta Mater.* 44: 905–910.

Eisenbarth, E., Velten, D., Muller, M., Thull, R. & Breme, J. (2004). Implications of metallic corrosion in total knee arthroplasty, *Biomaterials* 25: 5705–5713.

Fedotov, S. (1973). Peculiarities of changes in elastic properties of titanium martensite, *in* R. Jaffee & H. Burte (eds), *Titanium Science and Technology (Proc. 2nd Int. Conf. on Titanium)*, Plenum Press, New York, pp. 871–881.

Froimson, M. I., Garino, J., Machenaud, A. & Vidalain, J. P. (2007). Minimum 10-year results of a tapered, titanium, hydroxyapatite-coated hip stem, *J. Arthroplasty* 22: 1–7.

Gao, X., Huang, M. & Brinson, L. (2000). A multivariant micromechanical model for SMAs: part 1. crystallographic issues for single crystal model, *Int. J. Plast.* 16: 1345–1369.

Geetha, M., Singh, A., Asokamani, R. & Gogia, A. (2009). Ti based biomaterials, the ultimate choice for orthopaedic implants – a review, *Prog. Mater. Sci.* 54: 397–425.

Guo, Z., Fu, J., Zhang, Y., Hu, Y., Wu, Z., Shi, L., Sha, M., Li, S., Hao, Y. & Yang, R. (2009). Early effect of Ti–24Nb–4Zr–7.9Sn intramedullary nails on fractured bone, *Mater. Sci. Eng.*

C 29: 963–968.
Hao, Y., Li, S., Sun, B., Sui, M. & Yang, R. (2007). Ductile titanium alloy with low Poisson's ratio, *Phys. Rev. Lett.* 98: 216405.
Hao, Y., Li, S., Sun, S. & Yang, R. (2006). Effect of Zr and Sn on Young's modulus and superelasticity of Ti–Nb-based alloys, *Mater. Sci. Eng. A* 441: 112–118.
Hao, Y., Li, S., Sun, S., Zheng, C., Hu, Q. & Yang, R. (2005). Super-elastic titanium alloy with unstable plastic deformation, *Appl. Phys. Lett.* 87: 091906.
Hao, Y., Li, S., Sun, S., Zheng, C. & Yang, R. (2007). Elastic deformation behaviour of Ti–24Nb–4Zr–7.9Sn for biomedical applications, *Acta Biomater.* 3: 277–286.
Hao, Y., Li, S. & Yang, R. (2008). Nanostructured titanium alloys for implant applications, *in* D. Reisner (ed.), *Bionanotechnology: Global Prospects*, Chapter 5, CRC Press, New York, pp. 61–70.
Heinen, R., Hackl, K., Windl, W. & Wagner, M. (2009). Microstructural evolution during multiaxial deformation of pseudoelastic NiTi studied by first-principles-based micromemicromechanical modeling, *Acta Mater.* 57: 3856–3867.
Hu, Q., Li, S., Hao, Y. & Yang, R. (2008). Phase stability and elastic modulus of Ti alloys cotaining Nb, Zr, and/or Sn from first principles calculations, *Appl. Phys. Lett.* 93: 121902.
Li, S., Cui, T., Hao, Y. & Yang, R. (2008). Fatigue properties of a metastable β-type titanium alloy with reversible phase transformation, *Acta Biomater.* 4: 305–317.
Li, S., Zhang, Y., Sun, B., Hao, Y. & Yang, R. (2008). Thermal stability and mechanical properties of nanostructured Ti–24Nb–4Zr–7.9Sn alloy, *Mater. Sci. Eng. A* 480: 101–108.
Long, M. & Rack, H. (1999). Titanium alloys in total joint replacement – a materials science perspective, *Biomaterials* 19: 1621–1639.
Matsumoto, H., Watanabe, S. & Hanada, S. (2005). Beta TiNbSn alloys with low youngs modulus and high strength, *Mater. Trans.* 46: 1070–1078.
Nag, S., Banerjee, R. & Fraser, H. L. (2005). Microstructural evolution and strengthening mechanisms in Ti–Nb–Zr–Ta, Ti–Mo–Zr–Fe and Ti–15Mo biocompatible alloys, *Mater. Sci. Eng. C* 25: 357–362.
Niinomi, M. (2002). Recent metallic materials for biomedical applications, *Metall. Mater. Trans. A* 33: 477–486.
Niinomi, M. (2003). Fatigue performance and cyto-toxicity of low rigidity titanium alloy, *Biomaterials* 24: 2673–2683.
Nitta, K., Watanabe, S., Masahashi, N., Hosoda, H. & Hanada, S. (2004). Ni-free Ti–Nb–Sn shape memory alloys, *in* M. Niinomi (ed.), *Structural Biomaterials for the 21st Century*, TMS, Warrendale, PA, pp. 25–34.
Obbard, E. (2010). *Superelasticity in biomedical β titanium alloys*, Ph.D. Thesis, Institute of Metal Research, Chinese Academy of Sciences, Shenyang.
Obbard, E., Hao, Y., Akahori, T., Talling, R., Niinomi, M., Dye, D. & Yang, R. (2010). Mechanics of superelasticity in Ti–30Nb–(8–10)Ta–5Zr alloy, *Acta Mater.* 58: 3557–3567.
Obbard, E., Hao, Y., Talling, R., Li, S., Zhang, Y., Dye, D. & Yang, R. (2011). The effect of oxygen on α'' martensite and superelasticity in Ti–24Nb–4Zr–8Sn, *Acta Mater.* 59: 112–125.
Petry, W., Heiming, A., Trampenau, J., Alba, M., Herzig, C. & Vogl, H. R. S. G. (1991). Phonon dispersion of the bcc phase of group IV metals: I. bcc titanium, *Phys. Rev. B* 43: 10933.
Puska, A. & Golovin, S. (1985). *Fatigue in materials: cumulative damage processes*, Elsevier, Amsterdam.

Song, Y., Xu, D., Yang, R., Li, D., Wu, W. & Guo, Z. (1999). Theoretical study of the effects of alloying elements on the strength and modulus of β-type bio-titanium alloys, *Mater. Sci. Eng. A* 260: 269–274.

Song, Y., Yang, R., Li, D., Wu, W. & Guo, Z. (1999). Calculation of theoretical strengths and bulk moduli of bcc metals, *Phys. Rev. B* 59: 14220.

Tao, X., Li, S., Zheng, C., Fu, J., Guo, Z., Hao, Y., Yang, R. & Guo, Z. (2009). Synthesis of a porous oxide layer on a multifunctional biomedical titanium by micro-arc oxidation, *Mater. Sci. Eng. C* 29: 1923–1934.

Wan, Z., Dorr, L. D., Woodsome, T., Ranawat, A. & Song, M. (1999). Effect of stem stiffness and bone stiffness on bone remodeling in cemented total hip replacement, *J. Arthroplasty* 14: 149–158.

Wang, K. (1996). The use of titanium for medical applications in the USA, *Mater. Sci. Eng. A* 213: 134–137.

Wapner, K. (1991). Implications of metallic corrosion in total knee arthroplasty, *Clin. Orthop. Relat. Res.* 271: 12–20.

Zhang, Y. (2010). *Elastic and plastic deformation of Ti2448 single crystals*, Ph.D. Thesis, Institute of Metal Research, Chinese Academy of Sciences, Shenyang.

Zheng, C. (2009). *An investigation on the biocompatibility of* T*i–24*N*b–4Zr–8*S*n alloy*, Ph.D. Thesis, Institute of Metal Research, Chinese Academy of Sciences, Shenyang.

Zheng, C., Li, S., Tao, X., Hao, Y. & Yang, R. (2009). Surface modification of Ti–Nb–Zr–Sn alloy by thermal and hydrothermal treatments, *Mater. Sci. Eng. C* 29: 1245–1251.

Zheng, C., Li, S., Tao, X., Hao, Y., Yang, R. & Zhang, L. (2007). Calcium phosphate coating of Ti–Nb–Zr–Sn titanium alloy, *Mater. Sci. Eng. C* 27: 824–831.

Zhu, Y., Li, F., Li, S., Hao, Y. & Yang, R. (2009). Effect of elastic modulus on biomechanical properties of lumbar interbody fusion cage, *J. Mater. Sci. Technol.* 25: 325–328.

Biomedical Engineering, Trends in Materials Science

Edited by Mr Anthony Laskovski

ISBN 978-953-307-513-6
Hard cover, 564 pages
Publisher InTech
Published online 08, January, 2011
Published in print edition January, 2011

Rapid technological developments in the last century have brought the field of biomedical engineering into a totally new realm. Breakthroughs in materials science, imaging, electronics and, more recently, the information age have improved our understanding of the human body. As a result, the field of biomedical engineering is thriving, with innovations that aim to improve the quality and reduce the cost of medical care. This book is the second in a series of three that will present recent trends in biomedical engineering, with a particular focus on materials science in biomedical engineering, including developments in alloys, nanomaterials and polymer technologies.

INTECH
open science | open minds

InTech Europe
University Campus STeP Ri
Slavka Krautzeka 83/A
51000 Rijeka, Croatia
Phone: +385 (51) 770 447
Fax: +385 (51) 686 166
www.intechopen.com

InTech China
Unit 405, Office Block, Hotel Equatorial Shanghai
No.65, Yan An Road (West), Shanghai, 200040, China
中国上海市延安西路65号上海国际贵都大饭店办公楼405单元
Phone: +86-21-62489820
Fax: +86-21-62489821